Appl. Phys. A 81, 1559–1567 (2005)
DOI: 10.1007/s00339-005-3338-6

**Applied Physics A**
**Materials Science & Processing**

Invited paper

S. HOFMANN[1,✉]
M. CANTORO[1]
M. KAEMPGEN[2]
D.-J. KANG[3,5]
V.B. GOLOVKO[4]
H.W. LI[3,4]
Z. YANG[3,4]
J. GENG[4]
W.T.S. HUCK[3,4]
B.F.G. JOHNSON[4]
S. ROTH[2]
J. ROBERTSON[1]

# Catalyst patterning methods for surface-bound chemical vapor deposition of carbon nanotubes

[1] Department of Engineering, Cambridge University, Cambridge, CB2 1PZ, UK
[2] Max-Planck-Institut für Festkörperphysik, 70569 Stuttgart, Germany
[3] Nanoscience Centre, Cambridge University, Cambridge, CB3 0FF, UK
[4] Department of Chemistry, Cambridge University, Cambridge, CB2 1EW, UK
[5] Sungkyunkwan Advanced Institute of Nanotechnology, and Department of Physics, Sungkyunkwan University, Suwon 440-746, Korea

**Received: 20 June 2005/Accepted: 27 June 2005**
**Published online: 14 September 2005 •** 

**ABSTRACT** We present three different catalyst preparation and patterning techniques for plasma-enhanced chemical vapor deposition of carbon nanostructures from acetylene and ammonia mixtures. The different merits and potential areas of application are highlighted for each technique as compared to the benchmark of e-beam-lithography patterning. Maskless, focused ion beam written Pt can nucleate aligned carbon nanofibers, thereby allowing a sub-100 nm lateral resolution on non-planar substrate geometries combined with an in-situ monitoring. Ion beam milling additionally enables the pre-shaping and marking of the substrate, which is shown for the growth of individual nanofibers on the apex of commercial scanning probe tips. Pulsed electrochemical deposition was used to form Ni and Fe catalyst islands of controlled size and density. This is also demonstrated on complex substrate geometries such as carbon cloth. Nanocontact printing was employed to deposit a highly purified Co colloid in regular patterns with feature sizes down to 100 nm onto silicon wafers for low cost patterning over large areas. We analyze the catalyst restructuring upon exposure to elevated temperatures for each technique and relate this to the nucleated nanofiber dimensions and array densities. The flexibility in catalyst and substrate material allows a transfer of our achievements to catalyst-assisted growth of nanostructures in general facilitating their hierarchical device integration and future application.

**PACS** 81.16.Rf; 81.16.Hc; 61.46.+w

## 1 Introduction

The increasing range of nanomaterials promises the ability to build new bottom-up device architectures which utilize their novel, nanoscale properties [1, 2]. However, the ability to assemble and align such nanoscale building blocks in a controllable fashion presently poses a limit on applications. Bulk growth techniques such as arc-discharge [3] or laser ablation [4] tend to create a deposit of impure, entangled nanotubes or -wires, which leaves the challenge of post-growth purification, manipulation and assembly.

In contrast, chemical vapor deposition (CVD) [5, 6] not only allows a scalable process design but also enables controlled surface-bound growth easing future device integration. The selective and aligned growth of nanotubes/-wires/-fibers can be achieved directly on the substrate by means of pre-patterning a suitable catalyst [7] and exploiting epitaxial substrate orientation [8], applying an electrical field [9] or plasma [10] during growth. This circumvents a costly and time-consuming post-growth manipulation.

The current benchmark method for high resolution patterning is e-beam lithography, which can have a precision of a few nanometers [11]. However, e-beam writing ideally requires substrate planarity and its (presently) serial nature makes e-beam writing a high cost, low throughput method. This narrows its general utility for the catalytic CVD of nanostructures.

In this paper, we present three different catalyst preparation and patterning techniques highlighting their specific merits and the potential areas of application. The results are aimed at illustrating general aspects of the surface-bound growth of nanostructures [12, 13]. We use plasma enhanced (PE) CVD to convert the respective catalyst pattern into a corresponding array of vertically aligned carbon nanofibers (CNFs) and nanotubes (CNTs) [14].

First, we introduce the maskless, direct writing of a Pt catalyst film by focused ion beam (FIB) assisted deposition. FIB catalyst film writing gives a sub-100 nm lateral resolution with a controlled deposition rate. Unlike most other patterning techniques, FIB deposition allows a non-planar substrate geometry and an in-situ monitoring of the resulting layer, particularly in a dual-beam set-up. We also show that the pre-shaping of the substrate by FIB milling is a useful option, e.g., for the direct growth of CNF onto atomic force microscopy (AFM) tips.

Second, for the demand of low-cost and scalability, we studied pulsed electrochemical deposition to deposit the catalyst metal with controlled site density, as demonstrated by Tu et al. [15]. We show how annealing restructures the as-plated metal islands and how the diameter and site-density of the re-

✉ Fax: +44-1223-332662, E-mail: sh315@cam.ac.uk

sulting CNFs/CNTs varies according to the generated metal island distribution. For high plating pulse currents, we find the results to overlap with our previous data on the surface coarsening and growth of CNTs from evaporated and sputtered thin films [16]. We show that electroplating can also give a controlled site-density on complex three-dimensional substrates, such as carbon cloth.

Third, we report on the nanocontact printing of a purified, monodisperse cobalt colloid [17–20], which combines low-cost, large area with specific high-resolution patterning attributes. The stamp design was optimized enabling printed feature sizes in the 100 nm – scale, small enough to nucleate arrays of individual, free-standing CNFs or lines thereof. The latter result was published previously [20], however, is added here to help this article form a comparative overview of different catalyst systems and their patterning possibilities.

## 2 Experimental details

We used polished n-type Si(100) substrates unless stated otherwise. Pt was written by a $Ga^+$ focused ion beam (Philips Electron Optics/FEI Corporation 200 xP®FIB workstation) from a commercial organometallic precursor (trimethyl-methylcyclopentadienyl-platinum, $[(CH_3)_3CH_3C_5H_4Pt]$). The ion-assisted deposition was optimized at a $Ga^+$ current density of $\sim 4\,pA/\mu m^2$ at 30 kV and the dwell time was 0.5 μs per pixel with −50% overlap. The Pt thickness is estimated from a calibrated deposition rate.

Electroplating was carried out in a three electrode setup at room temperature. We used potentiostatic deposition in pulse mode to achieve small catalyst islands. Si substrates were pretreated for 10 s in an $NH_4F$ etchant (AF 87.5-12.5, Merck) to remove the native oxide. The samples were subsequently rinsed in water/isopropanol, clamped and immersed into the electrochemical cell. For Ni deposition we used aqueous 0.01 M $NiSO_4$ in 0.1 M $H_3BO_4$, Fe was deposited from 0.01 M $FeSO_4$ in 0.1 M $H_3BO_4$. The potential was controlled with a potentiostat (Jaissle, IMP 83 PC) connected to a pulse generator (Philips 5715). We used 10 ms pulses at −3 V versus a saturated calomel electrode (SCE) as the reference electrode. The samples were rinsed in water/isopropanol and characterized by atomic force microscopy (AFM; Nanoscope IIIa, Digital instruments).

For nanocontact-printing, an AOT (bis(2-ethylhexyl)sulfo succinate sodium salt) stabilized Co colloid was prepared by a modified "inverse micelle" method previously reported by Chen et al. [21]. The temperature during the reduction of the $Co^{2+}$ to Co metal was controlled by an ice-acetone bath, as elevated temperatures may lead to larger particle sizes [22]. Excess surfactant was removed by flocculating the colloid with methanol. Filtration through a 0.2 μm PTFE syringe filter and centrifugation (14 000 rpm, 1–4 min) gave a further purification and allowed a narrowing of the particle size distribution. High resolution transmission electron microscopy (HRTEM, JEOL 3010, 300 kV) analysis confirmed the presence of monodisperse crystalline Co nanoparticles with a diameter of 2–4 nm. The poly-dimethyl siloxane (PDMS) stamps consist of a 30–50 μm thick film of hard PDMS to reproduce sub-100 nm features, and a 5–10 mm layer of soft PDMS in order to facilitate printing over a large area [19]. Inked with Co colloid, the stamp was dried under $N_2$ flow and brought in contact with the silicon wafer for 5–30 s.

The vertically aligned CNFs were then grown using a DC PECVD system in a stainless steel vacuum chamber with a base pressure below $10^{-6}$ mbar. Details of the PECVD process are given elsewhere [14, 16]. The as-deposited catalyst patterns were transferred in air to the vacuum chamber, pumped down to base pressure, and then heated up in 0.6 mbar $NH_3$ (electronic grade) for 15 min to reach the desired growth temperature. A DC plasma discharge was generated by applying a 600–700 V bias between the graphite heater stage and an anode located ∼ 3 cm above. The acetylene feed gas, $C_2H_2$ (grade 1.5), was introduced via a separate mass flow controller. The $C_2H_2$:$NH_3$ ratio was kept constant at 50 : 200 sccm at a total pressure of 0.7 mbar and a typical discharge current of 20–30 mA, corresponding to a plasma power of typically less than 20 W. The temperature was continuously monitored by multiple thermocouples on reference substrates distributed across the heater stage.

The dimensions and structure of as-grown CNF arrays were analysed by scanning electron microscopy (SEM; JEOL 6340 FEGSEM, LEO 1530VP FEGSEM), HRTEM (Jeol JEM 4000EX, 400 kV) and Raman spectroscopy (Renishaw 1000 spectrometer, 514.5 nm excitation). The CNFs were removed from the substrates for HRTEM analysis and dispersed onto Cu TEM grids.

## 3 Results and discussion

### 3.1 *Focused ion beam deposition*

In order to deposit metal using a focused ion beam, an organometallic precursor gas is injected into the vacuum chamber through a needle near the substrate surface. The gas adsorbs on the surface and decomposes under the scanned ion beam to leave the deposited metal, as illustrated in Fig. 1. The FIB deposited Pt film can have a high concentration of contaminants such as Ga and carbon, due to the ion beam exposure and to the decomposition by-products of the organometallic precursor [23]. Typical resistivities for this material can range from 70 μΩ/cm to over 1000 μΩ/cm [24] whereas the bulk resistivity of pure Pt is 10 μΩ/cm [25]. The film thickness can be controlled by beam parameters and exposure time. Although the substrate should be reasonably conductive to avoid charging effects, as in SEM analysis, FIB has hardly any restrictions on substrate geometry [26].

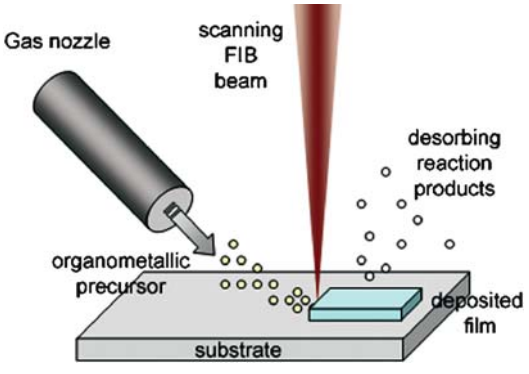


**FIGURE 1** Schematic of FIB induced thin film deposition

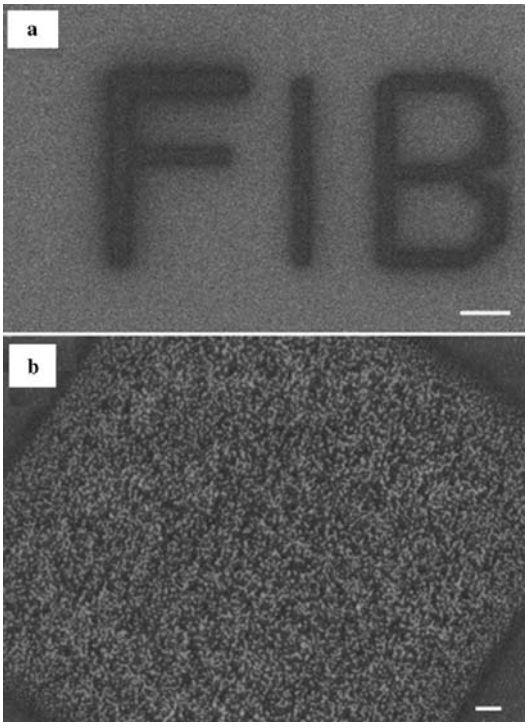


**FIGURE 2** (**a**) FIB deposited Pt pattern (scale bar 2 μm). (**b**) Pt square pattern after thermal annealing at 500 °C in $NH_3$ atmosphere (scale bar 200 nm)

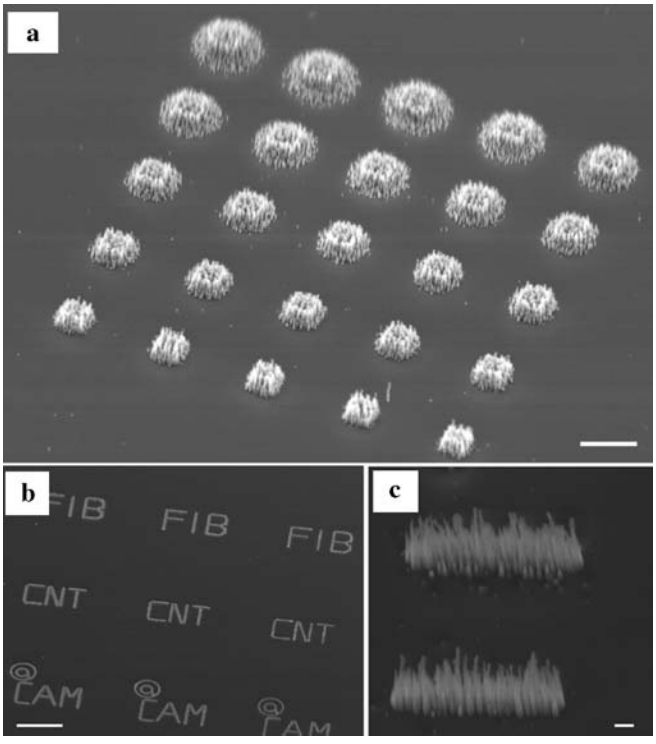


**FIGURE 3** SEM imaging of CNFs grown from FIB deposited Pt on $SiO_2$ barrier: (**a**) patterned $5 \times 5$ array of 500 $nm^2$ squares of decreasing Pt thickness (nominally 30–2 nm) processed in 1 : 4 $C_2H_2$ : $NH_3$ flow at 600 V DC bias, 530 °C for 30 min. FIB written (**b**) complete pattern (see Fig. 2a) and (**c**) individual 2 nm thick Pt lines exposed to 1 : 4 $C_2H_2$ : $NH_3$ flow at 700 V DC bias, 500 °C for 1 h (scalebars 1 μm, 10 μm, 100 nm, respectively)

Here, software-controlled Pt patterns of different thickness were directly written onto untreated and thermally oxidized Si. An exemplary Pt pattern is shown in Fig. 2a. Typically, as-deposited metal films nucleate in a Volmer–Weber mode, i.e., can be discontinuous for very low thicknesses. Upon annealing and/or plasma pre-treatment, the metal film roughens and (depending on its thickness) breaks up into a discontinuous island topography Fig. 2b. This agglomeration is driven by a surface and elastic energy minimization, enabled by a greater surface mobility [27, 28]. As observed for thin film catalysts in general [16], the average metal island size typically increases with initial film thickness and with the annealing temperature [29]. The onset temperature for the thermally induced structural transformations [30] and surface restructuring can thereby be very low. For the significant coarsening of nm-thick transition metal films on Si-based substrates we find an onset below 300 °C. A plasma pre-treatment can additionally modify the topology of the catalyst film [16], typically enhancing the CNF nucleating density by a preferential etching at the grain boundaries [31]. An as-formed catalyst island size represents an upper limit to the subsequently grown nanotube/-fiber diameter. The detailed nature of the nucleating nanostructure, however, critically depends on the process conditions.

Figure 3 shows CNF arrays grown from Pt films of various thicknesses under DC PECVD conditions. The carbon nanostructures nucleate selectively from the catalyst pattern. The ammonia dilution prevents amorphous carbon deposition on the surrounding Si substrate, as probed by Raman spectroscopy [32]. Direct FIB catalyst writing can give lateral feature sizes small enough to nucleate individual lines of CNFs Fig. 3c. Nominally 2 nm thick Pt catalyzed a CNF diameter distribution centered around 30–40 nm Fig. 3c. Compared to Ni, Co and Fe catalysts [16], the CNFs appear rather short and tapered with a length typically not exceeding 500 nm. For thicker Pt the average CNF diameter increases and the distribution widens Fig. 3a. The halo present for thick Pt films is FIB deposition related. Within a nominal Pt thickness variation of 30–2 nm the terminal nanofiber length remained roughly constant. Smaller pattern sizes and a deposition time exceeding 30 min also gave no increase in fiber length, indicating an early saturation, i.e., poisoning of the catalyst.

Pt is known as active catalyst increasing the rates of reaction in fuel cells. Hence its catalytic role in CNF growth is interesting as its presence would not introduce another metal impurity when CNFs are used to increase the electrode area in polymer membrane fuel cells [33].

Despite progress reported in the literature, the detailed role of the metal catalyst in the CVD of CNTs and CNFs is not fully understood [34]. E-beam evaporated Pt was shown to catalyze the growth of CNFs of μm-length and 40–170 nm diameter, whereby an $NH_3$ plasma pre-treatment and increased temperature were shown to be beneficial [35]. Pt on silicon support exhibits a tip-growth regime in these conditions, similar to Ni, Co and Fe catalyst films [16, 35]. It is likely that the present growth from FIB deposited Pt can be further optimized in terms of growth conditions, catalyst pretreatments and the diffusion characteristics of the support layers. Considering the rapid development of FIB technology, it can also be expected that the range of metals for direct writing will widen, introducing more catalyst precursors for the presented process. FIB ion beam implantation combined with

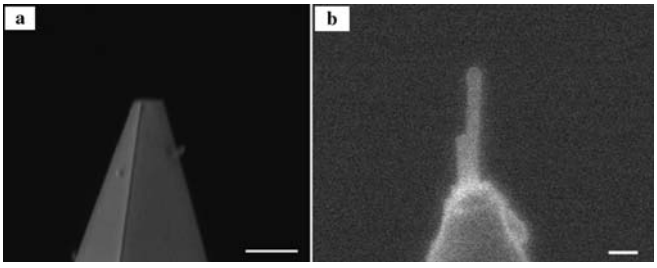


**FIGURE 4** SEM micrographs of (**a**) FIB cut AFM tip, (**b**) as-grown CNFs at apex after Ni catalyst deposition and resist lift-off. Growth conditions: 1 : 4 $C_2H_2$ : $NH_3$ flow at 600 V DC bias, 500 °C for 20 min (scalebars: 1 μm, 100 nm, respectively)

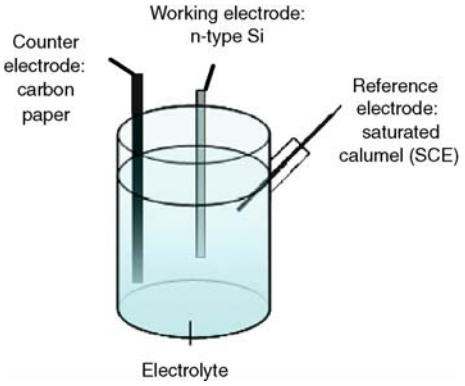


**FIGURE 5** Schematic of the three electrode set-up used for pulsed electroplating

subsequent annealing can give site-controlled Ga nanodots, which themselves can act as nucleation sites for growth of nanowires [36].

The FIB can also be utilized for catalyst preparation in its milling mode. Figure 4 shows an example of such a FIB based procedure. It is highly desirable to be able to grow aligned nanostructures at the apex of scanning probe tips in order to improve the resolution and functionality of scanning probe microscopy (SPM) [37]. Growing CNTs/CNFs for SPM probes requires a robust anchoring of the nanostructure to the cantilever and an accurate control over structural dimensions such as length, to avoid vibrational broadening [38]. Here, either the AFM cantilever tip itself and/or a protective resist overcoat have been partly removed by FIB milling Fig. 4a. After Ni sputtering and subsequent resist lift-off, the as-prepared blunting/masking left a catalyst island supported on a small plateau at the apex. PECVD growth then resulted in free-standing CNFs aligned perpendicular to the cut plateau surface Fig. 4b. As-grown CNF show a good anchoring to the substrate [39] with a length that is tuneable by the deposition time. Tip-growth results in a small metal inclusion at the apex, potentially interesting for near-field scanning optical or magnetic force microscopy. The PECVD tips are currently being tested as probes for different scanning techniques, including various functionalizations for chemical force microscopy. FIB processing, however, does require relatively expensive equipment. It is also a serial writing process, so it is slow for large areas. We, therefore, investigated other techniques of controlled catalyst deposition; electroplating and printing.

### 3.2 *Pulsed electrochemical deposition*

Figure 5 illustrates the three electrode set-up used for electroplating. Electrodeposition is a widely used industrial production method capable of producing high quality metal films [40, 41]. Plating does not depend on substrate planarity, in fact the conformal coverage allows the filling of cavities and pores. As the substrate should be electrically conductive, selective electrodeposition can be achieved by varying the conductivity of the substrate [42], at preferential sites such as defects [43] or on conductive (nano)templates, e.g., CNTs [44]. As a similar method, electroless plating requires no electrical current and thus no substrate conductivity but it does require a catalyzing surface and it is, therefore, limited to certain combinations between metals and substrates [45, 46]. Localized plating can also be achieved based on a scanning operation of miniaturized, needle-like electrodes [47]. The nucleation of electroplated films proceeds in a Volmer–Weber mode, starting as separate islands. Therefore, the growth process, if stopped early, can give a catalyst island pattern of controlled site density. A pulsed operation enables a kinetic controlled nucleation from diffusion controlled growth and therefore allows the preparation of small particles with a narrow size distribution [43]. Further, this method gives enhanced control in terms of pulse amplitude, duration and pulse count.

Figure 6 shows AFM images of Ni nanoparticles deposited by electroplating with different pulse parameters resulting in different site densities. The detailed pulse values required depend on the molar concentration of the electrolyte. Electroplating was successful directly onto doped Si substrates, whereby homogeneity is more easily achieved when using a metallic underlayer such as Cr [15]. Figure 6a shows a typical as-plated Ni island size distribution: larger Ni islands with an average lateral extension exceeding 150 nm coexist with Ni nanoparticles smaller than 30 nm. The distribution is similar to Tu et al., who describe Ni nanoparticle site-densities from $7.5 \times 10^5$ to $3 \times 10^8$ $cm^{-2}$ [15].

Figure 7a shows a close-up of a high site density at the transition of forming a continuous Ni layer. Regarding the conversion of the electroplated site density into CNF patterns, it should be emphasised that the plated nano-islands restructure upon annealing (compare to Fig. 2b). Figure 7b shows the sintering of the previously shown film Fig. 7a for a thermal annealing at 500 °C. Islands are formed roughly 150 nm in lateral extent, giving a very different surface topography for seeding CNF growth. For lower Ni island densities, the degree of sintering depends on the island spacing, surface interactions and Ni mobility [27]. Without the use of a barrier, silicide formation with the substrate has to be considered [48]. Although the annealing was performed in vacuum or a controlled atmosphere, the AFM measurements were performed at ambient conditions; therefore, a (for Ni minor) surface oxidization is present. It should also be noted that a strict 1 : 1 correlation between the initial catalyst island size and the CNT/CNF diameter is not necessarily expected. Regarding CNF nucleation, for instance, it depends on the deformation of the catalyst during nucleation [39, 49] into the typical, long conical droplets seen by HRTEM [16].

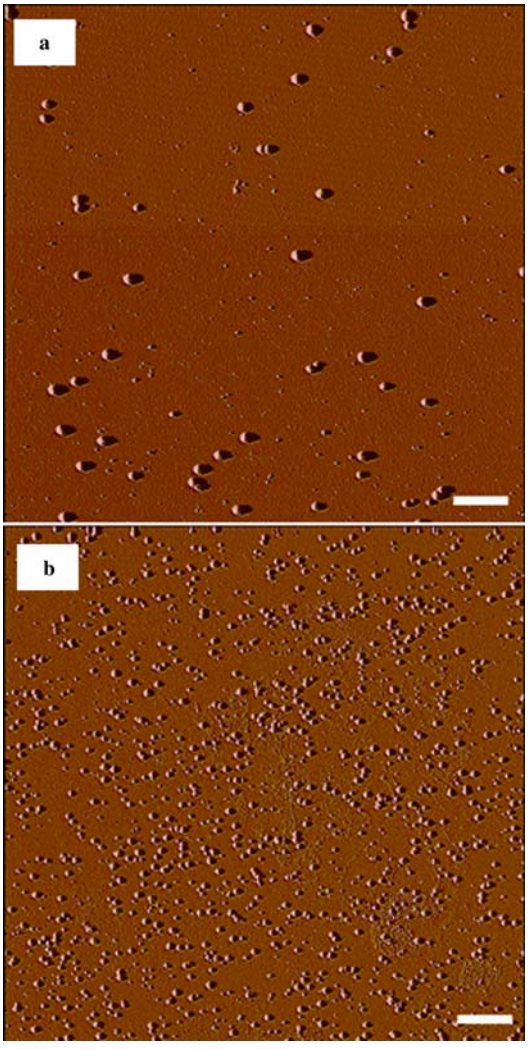


**FIGURE 6** AFM analysis of electroplated Ni islands on Si with different pulse repetition: (**a**) 1, (**b**) 10 times (scalebars 1 μm)

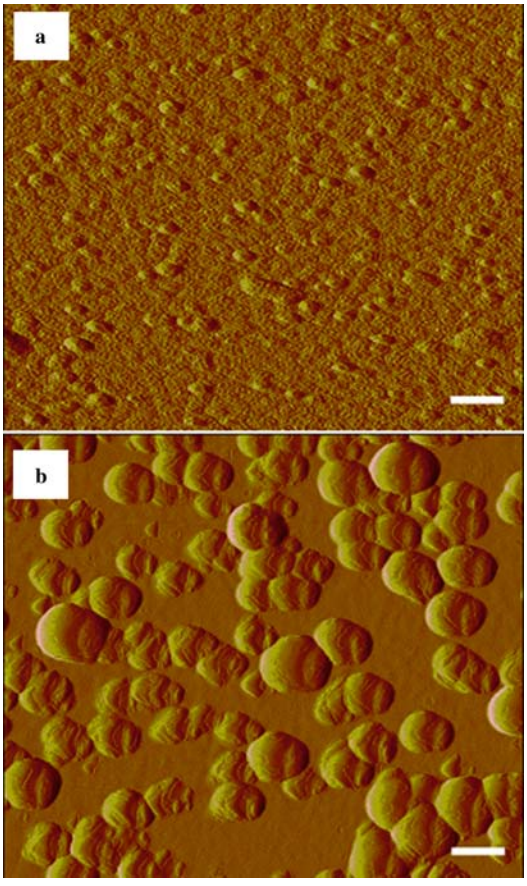


**FIGURE 7** AFM images of (**a**) as-plated Ni islands (5 V pulse, 10 times repetition), (**b**) Ni island distribution after thermal annealing at 500 °C in vacuum (scalebars 100 nm)

Figure 8 shows SEM images of plasma aligned CNFs grown from the various plated catalyst films. Although no extended plasma pre-etching was used, very small catalyst clusters (< 5 nm) are found to be etched away by the plasma during deposition [16]. The site-density of the remaining (sintered) metal islands is reflected in the CNF density Fig. 8a,b. The CNF diameter distribution is centered around 40 nm, indirectly indicating the degree of catalyst restructuring and deformation. The nanofibers have a bamboo-like internal structure [14] and have a catalyst inclusion at their tip, indicating tip-growth. The CNF length depends on deposition time, and was observed to continuously increase for at least 1 h.

Figure 8c shows a thin electroplated Fe film after exposure to the $C_2H_2 : NH_3$ plasma. Very dense arrays of small diameter (∼ 5 nm) CNTs are formed, with an almost a factor 100 faster growth rate. This is similar to what we observe for sub-3 nm Fe layers prepared by evaporation or sputtering [16]. HRTEM shows that the CNTs consist of 2–5 graphitic shells and, although defective, no regularly spaced bamboo intersects are present [16]. The CNT alignment in this case is mainly due to on a crowding effect dominated by van-der-Waals interactions between neighbouring nanotubes. A similar bundling is well known for bulk production techniques such as arc-discharge and laser-ablation [3].

Under standard processing conditions, electroplated or evaporated/sputtered [16] Ni does not trigger such a fast growth of dense CNT arrays. As this CNF/CNT growth mode change is linked to the catalyst film coarsening and island formation, this generally underlines the importance of the catalyst restructuring during the initial heat-up and indicates the dependence on the metal used. Interestingly, we find that a pre-treatment of thin Ni films (2 nm) in a pure $NH_3$ discharge for 5 min before the introduction of acetylene can trigger the growth of CNT bundles similar to those found for Fe [16].

We observe a much faster catalyst poisoning for small diameter CNTs. Generally, catalyst poisoning is attributed to a progressive blocking of the active surface by excess amorphous carbon [50]. Despite the role of the plasma in etching away this blocking carbon, small catalyst clusters with a smaller active surface are likely to poison more quickly. It is interesting to note that, unlike in recent results on thermal growth in an ethylene/argon/water atmosphere [51], with the gas ratios used here, plasma etching could not prevent this deactivation.

Carbon cloth from Morgan Specialty Graphite consists of entangled carbon fibers ∼ 15 μm in diameter Fig. 9a. It is used here as typical substrate with a complex three-dimensional topography. Figure 9b shows that also in this case electroplating enables catalytic CNF growth with a controlled site density.

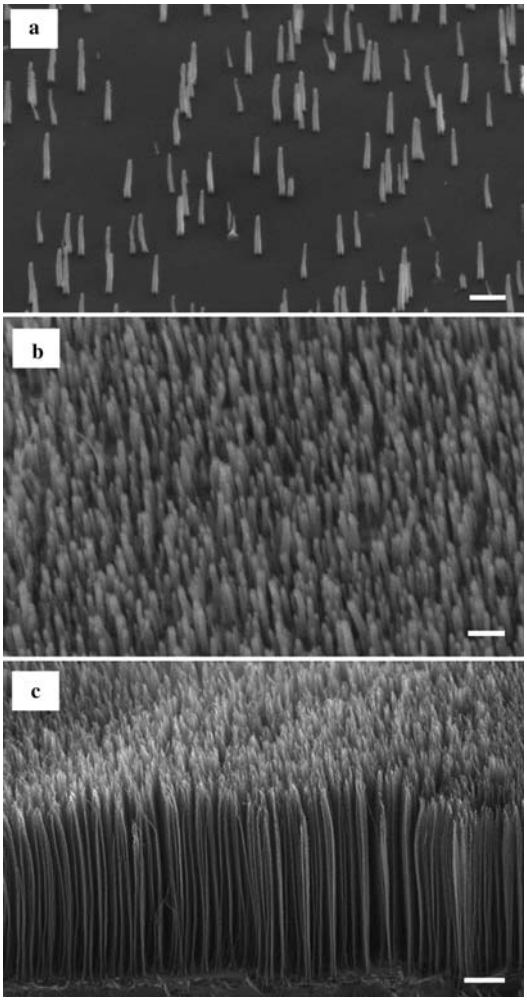


**FIGURE 8** SEM images of aligned CNFs catalysed by electroplated Ni islands of different density (**a**,**b**). (**c**) CNTs nucleated from electroplated Fe. Growth conditions: 1 : 4 $C_2H_2$ : $NH_3$ flow at 600 V DC bias, 550 °C for 15 min (scalebars: 200 nm, 200 nm, 5 μm, respectively)

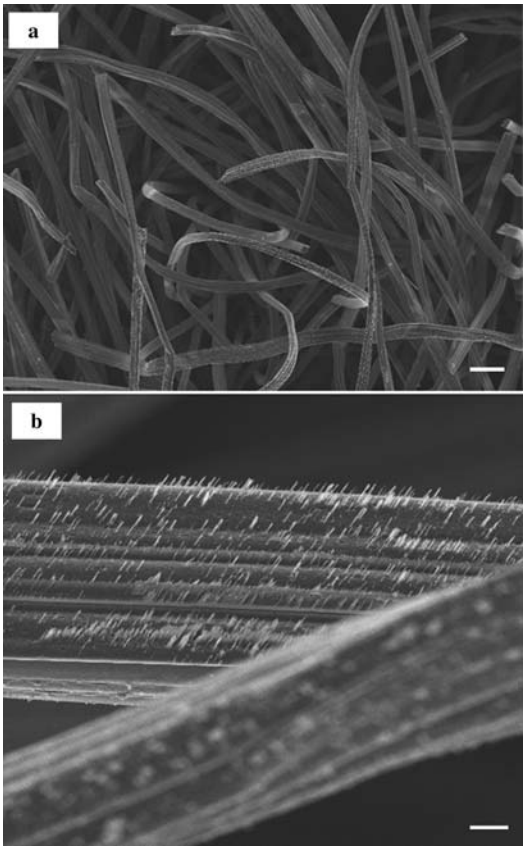


**FIGURE 9** SEM images of CNFs of controlled site density grown directly onto carbon cloth with electroplated Ni (5 V pulse). Growth conditions similar to Fig. 8 (scalebars 50 μm, 3 μm, respectively)

This approach is not limited to metal cluster growth on defect or active sites as required for electroless metal decoration of CNTs [52–54], which has been earlier used for catalyst deposition and subsequent CNT/CNF growth [55]. We observe the as-grown CNF dimensions and structural characteristics to be very similar to the growth on silicon support. It is interesting to note that no growth is observed in the absence of a carbon containing feed gas, indicating that the cloth substrate itself does not act as a solid carbon source at these conditions. A more detailed study of surface interactions is currently conducted. The total CNF coverage throughout the ∼ 2–3 mm thick cloth substrate can be improved by directing the gas flow through the cloth bulk [56]. The effectiveness of such growth of well anchored, aligned and non-bundled CNFs on complex surfaces is specifically aimed at electrode, fuel cell and supercapacitor applications.

### 3.3 *Nanocontact printing*

Figure 10 illustrates the principle of nanocontact printing. Dot and line patterned PDMS stamps Fig. 10a,b were fabricated by replica moulding from FIB milled or anisotropically etched Si master [19, 57, 58]. FIB processing thereby allows a rapid prototyping of more complex stamp masters. A freshly prepared and purified solution of Co colloid was used as ink. This has to be distinguished from methods where the adhesion agent rather than the colloid itself is patterned and the nanoparticles are subsequently deposited for instance by dipping [59]. The PDMS stamp was inked with colloid, blow dried ($N_2$) and brought in conformal contact with the substrate surface Fig. 10c. The stamp mass of 0.5–1 g was often sufficient to ensure contact during printing. Additional pressure can be exerted by hand or a controlled weight [20].

SEM images of as-printed catalyst patterns are shown in Fig. 11. The dot diameter or line width is dependent on the contact pressure and ink transfer. The printing process is not diffraction limited and in principle allows for a sub-50 nm resolution over large substrate areas [19, 60]. A high catalyst loading, however, smears the pattern leading to larger feature sizes. Regarding the subsequent CNF growth process, the catalyst size here was optimized to nucleate individual CNF or lines thereof, which roughly corresponds to printed feature sizes of 100–300 nm [20]. For typical conditions, as-patterned lines show a height of 30–60 nm in AFM analysis.

As with all other techniques, the catalyst behaviour during the pre-growth annealing is important. Unlike thin film catalysts where the film restructuring during annealing determines the catalyst island size distribution, colloidal precursors potentially offer a unique diameter control via the transfer

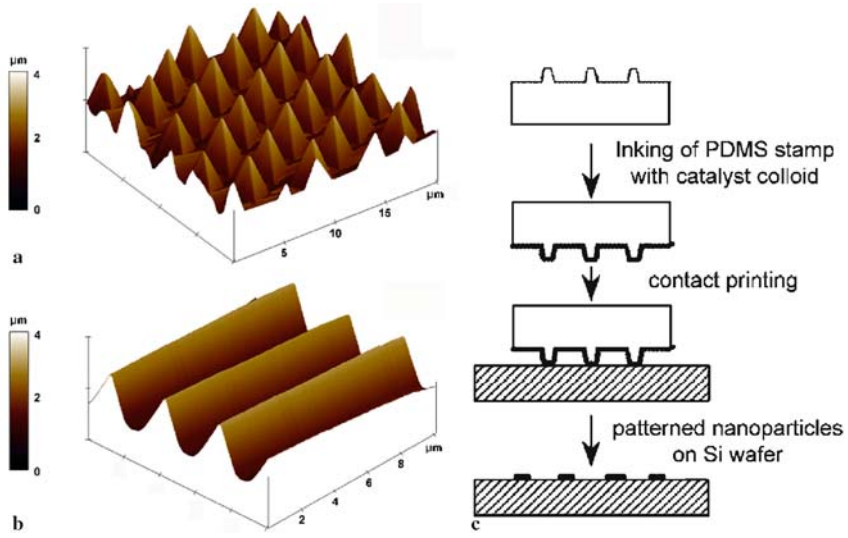


**FIGURE 10** Nanocontact printing: AFM images of (**a**) *dot* and (**b**) *line shaped* fabricated PDMS stamps. (**c**) Schematic of nanocontact printing process

of a chemically predefined size distribution [61]. Here, the average Co nanoparticle diameter was $\sim$ 2–4 nm [20]. However, once exposed to higher temperatures, the as-printed Co colloids loose their surfactant shell and, depending on their density, become prone to substrate-based sintering, cluster diffusion and Ostwald ripening [27, 62].

Figure 12 shows aligned CNFs grown using patterned Co colloid catalyst under DC PECVD conditions. The CNF arrays show good uniformity across cm-sized test samples. Depending on deposition temperature and the amount of printed colloid, the CNF diameter distribution is centered around 10–50 nm [18, 20]. This is indicative of the degree of restructuring of the Co nanoparticles during annealing and/or CNF growth, which is typically coupled to a shrinking of the printed feature sizes. An increasing deposition temperature up to $\sim$ 600 °C gives larger catalyst clusters and thus larger CNF diameters. We are currently investigating these sintering effects in more detail, thereby also including fast-heating procedures with heater stages of low thermal mass.

As for the previously presented catalysts, plasma etching is optimized for an amorphous carbon free background and thereby is found to clear small Co clusters and to heavily affect the remaining catalyst islands. Rutherford back-scatter (RBS) detection in the SEM and HREM analysis [18, 20] support a tip-growth regime and show a predominantly bamboo-like CNF crystallinity. The use of ammonia or nitrogen is often linked to C-N defect creation and impurity incorporation [63, 64]. Electron energy loss spectroscopy (EELS) of our

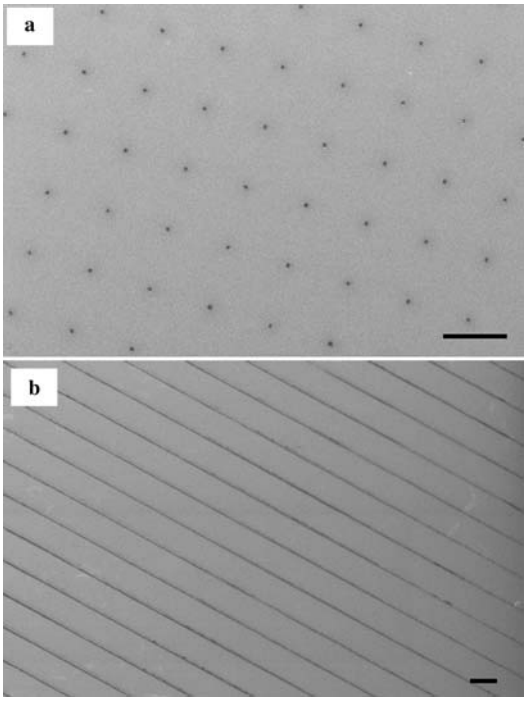


**FIGURE 11** SEM images of as-printed Co colloid (**a**) *dot* and (**b**) *line patterns* (scalebars 4 μm, 3 μm, respectively)

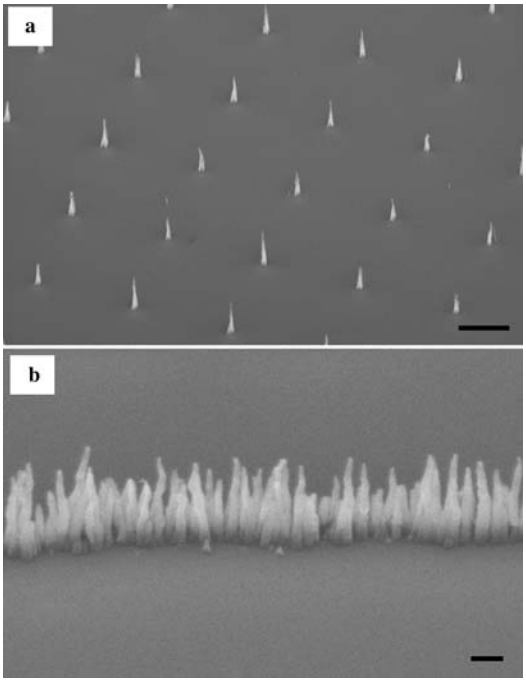


**FIGURE 12** SEM images of (**a**) *dot* and (**b**) *line patterned*, aligned CNF arrays. Growth conditions: 1 : 4 $C_2H_2$ : $NH_3$ flow at 600 V DC bias, 500 °C for 15 min (scalebars 2 μm, 100 nm, respectively)

plasma-aligned CNFs shows a very weak nitrogen signature indicative of a few atomic % N. We are presently screening various plasma and thermal growth conditions to elaborate on the variation of nanofiber/-tube crystallinity and the sources of bamboo-like intersect creation.

## 4 Conclusions

In conclusion, we have presented three different catalyst preparation and patterning techniques for surface-bound CVD of carbon nanostructures. We highlighted their different merits and potential areas of application compared to the benchmark set by e-beam-lithography. Maskless, direct catalyst deposition by FIB allows a sub-100 nm lateral resolution on non-planar substrate geometries combined with an in-situ monitoring of the resulting layer. Additionally, FIB milling enables the pre-shaping and marking of the substrate. Pulsed electrochemical deposition gives control over catalyst island size and density even on complex substrate geometries and provides scalability at high throughput and low cost. Nanocontact printing of a catalyst colloid allows large-area, uniform sub-300 nm patterning with flexible stamp manufacturing. Although we report on the growth of aligned carbon nanofibers/-tubes, the flexibility in catalyst and substrate material allows a transfer of our achievements to catalyst-assisted growth of nanostructures in general facilitating their hierarchical device integration and future application.

**ACKNOWLEDGEMENTS** We thank the EU Commission (CARDECOM, CANAPE) for funding, C. Ducati for HRTEM analysis, R.E. Dunin-Borkowski for EELS and B.O. Boskovic for supplying carbon cloth substrates. S.H. acknowledges support from Peterhouse, Cambridge.

## REFERENCES

1 M. Terrones, Annu. Rev. Mater. Res. **33**, 419 (2003)
2 Y.N. Xia, P.D. Yang, Y.G. Sun, Y.Y. Wu, B. Mayers, B. Gates, Y.D. Yin, F. Kim, Y.Q. Yan, Adv. Mater. **15**, 353 (2003)
3 S. Iijima, Nature **354**, 56 (1991)
4 A.M. Morales, C.M. Lieber, Science **279**, 208 (1998)
5 L.J.E. Hofer, E. Sterling, J.T. McCartney, J. Phys. Chem. **59**, 1153 (1955)
6 R.S. Wagner, W.C. Ellis, Appl. Phys. Lett. **4**, 89 (1964)
7 J. Kong, H.T. Soh, A.M. Cassell, C.F. Quate, H.J. Dai, Nature **395**, 878 (1998)
8 K. Hiruma, M. Yazawa, K. Haraguchi, K. Ogawa, T. Katsuyama, M. Koguchi, H. Kakibayashi, J. Appl. Phys. **74**, 3162 (1993)
9 H.B. Peng, T.G. Ristroph, G.M. Schurmann, G.M. King, J. Yoon, V. Narayanamurti, J.A. Golovchenko, Appl. Phys. Lett. **83**, 4238 (2003)
10 Z.F. Ren, Z.P. Huang, J.W. Xu, J.H. Wang, P. Bush, M.P. Siegal, P.N. Provencio, Science **282**, 1105 (1998)
11 S. Yasin, D.G. Hasko, H. Ahmed, Appl. Phys. Lett. **78**, 2760 (2001)
12 S. Hofmann, C. Ducati, R.J. Neill, S. Piscanec, A.C. Ferrari, J. Geng, R.E. Dunin-Borkowski, J. Robertson, J. Appl. Phys. **94**, 6005 (2003)
13 A. Colli, S. Hofmann, A.C. Ferrari, C. Ducati, F. Martelli, S. Rubini, S. Cabrini, A. Franciosi, J. Robertson, Appl. Phys. Lett. **86**, 153 103 (2005)
14 S. Hofmann, C. Ducati, J. Robertson, B. Kleinsorge, Appl. Phys. Lett. **83**, 135 (2003)
15 Y. Tu, Z.P. Huang, D.Z. Wang, J.G. Wen, Z.F. Ren, Appl. Phys. Lett. **80**, 4018 (2002)
16 S. Hofmann, M. Cantoro, B. Kleinsorge, C. Casiraghi, A. Parvez, J. Robertson, C. Ducati, J. Appl. Phys. 98, 034 308 (2005)
17 H. Ago, T. Komatsu, S. Ohshima, Y. Kuriki, M. Yumura, Appl. Phys. Lett. **77**, 79 (2000)
18 B. Kleinsorge, V.B. Golovko, S. Hofmann, J. Geng, D. Jefferson, J. Robertson, B.F.G. Johnson, Chem. Commun. **12**, 1416 (2004)
19 H.W. Li, B.V.O. Muir, G. Fichet, W.T.S. Huck, Langmuir **19**, 1963 (2003)
20 V.B. Golovko, H.W. Li, B. Kleinsorge, S. Hofmann, J. Geng, M. Cantoro, Z. Yang, D. Jefferson, B.F.G. Johnson, W.T.S. Huck, J. Robertson, Nanotechnology **16**, 1636 (2005)
21 J.P. Chen, K.M. Lee, C.M. Sorensen, K.J. Klabunde, G.C. Hadjipanayis, J. Appl. Phys. **75**, 5876 (1994)
22 D.P. Dinega, M.G. Bawendi, Angew. Chem. Int. Edit. **38**, 1788 (1999)
23 K.A. Telari, B.R. Rogers, H. Fang, L. Shen, R.A. Weller, D.N. Braski, J. Vac. Sci. Technol. B **20**, 590 (2002)
24 T. Tao, J.S. Ro, J. Melngailis, Z.L. Xue, H.D. Kaesz, J. Vac. Sci. Technol. B **8**, 1826 (1990)
25 D.R. Lide, *CRC handbook of chemistry and physics*, 79th ed. (Crc, Boca Raton, Fla.; London, 1998)
26 S. Reyntjens, R. Puers, J. Micromech. Microeng. **11**, 287 (2001)
27 J.M. Wen, J.W. Evans, M.C. Bartelt, J.W. Burnett, P.A. Thiel, Phys. Rev. Lett. **76**, 652 (1996)
28 E. Jiran, C.V. Thompson, Journal of Electronic Materials **19**, 1153 (1990)
29 C.A. Bower, O. Zhou, Zhu Wei, D.J. Werder, J. Sungho, Appl. Phys. Lett. **77**, 2767 (2000)
30 W. Lisowski, E.G. Keim, M. Smithers, Appl. Surf. Sci. **189**, 148 (2002)
31 Z.P. Huang, J.W. Wu, Z.F. Ren, J.H. Wang, M.P. Siegal, P.N. Provencio, Appl. Phys. Lett. **73**, 3845 (1998)
32 S. Hofmann, B. Kleinsorge, C. Ducati, A.C. Ferrari, J. Robertson, Diam. Relat. Mater. **13**, 1171 (2004)
33 C. Wang, M. Waje, X. Wang, J.M. Tang, R.C. Haddon, Y.S. Yan, Nano Lett. **4**, 345 (2004)
34 S. Hofmann, G. Csanyi, A.C. Ferrari, M.C. Payne, J. Robertson, Phys. Rev. Lett. **95**, 036 101 (2005)
35 J.H. Han, S.H. Choi, T.Y. Lee, J.B. Yoo, C.Y. Park, T. Jung, S.G. Yu, W. Yi, I.T. Han, J.M. Kim, Diam. Relat. Mat. **12**, 878 (2003)
36 R. Buckmaster, T. Hanada, Y. Kawazoe, M.W. Cho, T.F. Yao, N. Urushihara, A. Yamamoto, Nano Lett. **5**, 771 (2005)
37 H.J. Dai, J.H. Hafner, A.G. Rinzler, D.T. Colbert, R.E. Smalley, Nature **384**, 147 (1996)
38 L.A. Wade, I.R. Shapiro, Z.Y. Ma, S.R. Quake, C.P. Collier, Nano Lett. **4**, 725 (2004)
39 H.T. Cui, X.J. Yang, M.L. Simpson, D.H. Lowndes, M. Varela, Appl. Phys. Lett. **84**, 4077 (2004)
40 L.T. Romanikow, P.T. Palumbo, *Electrodeposition Technology, Theory and Practice*. (Electrochem. Soc., Pennington 1988)
41 P.C. Pearson, P.T. Moffat, Crit. Rev. Surf. Chem. **3**, 171 (1994)
42 C. Scheck, P. Evans, R. Schad, G. Zangari, L. Sorba, G. Biasiol, S. Heun, Appl. Phys. Lett. **86**, 133 108 (2005)
43 R.M. Penner, J. Phys. Chem. B **106**, 3339 (2002)
44 T.M. Day, P.R. Unwin, N.R. Wilson, J.V. Macpherson, J. Am. Chem. Soc. **127**, 10 639 (2005)
45 G.O. Mallory, J.B. Hajdu, *Electroless Plating: Fundamentals and Applications*. (AESF Orlando, 1990)
46 M. Liebau, E. Unger, G.S. Duesberg, A.P. Graham, R. Seidel, F. Kreupl, W. Hoenlein, Appl. Phys. A **77**, 731 (2003)
47 A. Jansson, G. Thornell, S. Johansson, J. Electrochem. Soc. **147**, 1810 (2000)
48 Y.J. Chang, J.L. Erskine, Phys. Rev. B **26**, 4766 (1982)
49 S. Helveg, C. Lopez-Cartes, J. Sehested, P.L. Hansen, B.S. Clausen, J.R. Rostrup-Nielsen, F. Abild-Pedersen, J.K. Norskov, Nature **427**, 426 (2004)
50 R.T.L. Baker, M.A. Barber, in *Chemistry and Physics of Carbon*, ed. by P.L. Walker, P.A. Thrower (Dekker, New York, 1978), Vol. 14
51 K. Hata, D.N. Futaba, K. Mizuno, T. Namai, M. Yumura, S. Iijima, Science **306**, 1362 (2004)
52 Y.W. Fan, M. Burghard, K. Kern, Adv. Mater. **14**, 130 (2002)
53 T.W. Ebbesen, H. Hiura, M.E. Bisher, M.M.J. Treacy, J.L. Shreeve-Keyer, R.C. Haushalter, Adv. Mater. **8**, 155 (1996)
54 R.Q. Yu, L.W. Chen, Q.P. Liu, J.Y. Lin, K.L. Tan, S.C. Ng, H.S.O. Chan, G.Q. Xu, T.S.A. Hor, Chem. Mat. **10**, 718 (1998)
55 E. Unger, G.S. Duesberg, M. Liebau, A.P. Graham, R. Seidel, F. Kreupl, W. Hoenlein, Appl. Phys. A **77**, 735 (2003)
56 M. Cantoro, V.B. Golovko, S. Hofmann, D.R. Williams, C. Ducati, J. Geng, B.O. Boskovic, B. Kleinsorge, D. Jefferson, A.C. Ferrari, B.F.G. Johnson, J. Robertson, Diam. Relat. Mat. **14**, 733 (2005)
57 H.W. Li, D.J. Kang, M.G. Blamire, W.T.S. Huck, Nanotechnology **14**, 220 (2003)
58 Y.N. Xia, G.M. Whitesides, Adv. Mater. **8**, 765 (1996)

59 T. Sato, D.G. Hasko, H. Ahmed, J. Vac. Sci. Technol. B **15**, 45 (1997)
60 F. Hua, Y.G. Sun, A. Gaur, M.A. Meitl, L. Bilhaut, L. Rotkina, J.F. Wang, P. Geil, M. Shim, J.A. Rogers, A. Shim, Nano Lett. **4**, 2467 (2004)
61 C.L. Cheung, A. Kurtz, H. Park, C.M. Lieber, J. Phys. Chem. B **106**, 2429 (2002)
62 N.C. Bartelt, W. Theis, R.M. Tromp, Phys. Rev. B **54**, 11 741 (1996)
63 J.H. Choi, S.H. Choi, J.H. Han, J.B. Yoo, C.Y. Park, T. Jung, S.G. Yu, I.T. Han, J.M. Kim, J. Appl. Phys. **94**, 487 (2003)
64 M. Glerup, M. Castignolles, M. Holzinger, G. Hug, A. Loiseau, P. Bernier, Chem. Commun. **20**, 2542 (2003)